AIAA JOURNAL
Vol. 38, No. 11, November 2000

Euler-Based Inverse Method for Turbomachine Blades, Part 2: Three-Dimensional Flows

T. Dang,* S. Damle,† and X. Qiu‡
Syracuse University, Syracuse, New York 13244

The aerodynamic design method for turbomachine blades reported in part 1 (Dang, T., and Isgro, V., "Euler-Based Inverse Method for Turbomachine Blades Part 1: Two-Dimensional Cascades," *AIAA Journal*, Vol. 33, No. 12, 1995, pp. 2309–2315) is extended to three dimensions. In this inverse method, the blade pressure loading (i.e., pressure difference between blade upper and lower surfaces) and the blade thickness distributions are prescribed, and the corresponding blade camber surface is sought. The inverse problem is formulated using a pressure-loading boundary condition across the blade surfaces, and modification of the blade geometry is achieved using the flow-tangency conditions along the blade surfaces. The method is demonstrated for the design of axial-flow machines ranging from the subsonic to the supersonic flow regimes.

Nomenclature

B = number of blades
c = speed of sound
f = blade wrap angle (or mean camber surface)
p = static pressure
T = blade thickness
V = absolute velocity
W = relative velocity
(r, θ, z) = cylindrical cordinate system
α = blade surface
Δp = blade pressure loading
ρ = density
ω = blade rotational speed

Superscripts

$+$ = blade upper surface
$-$ = blade lower surface

I. Introduction

RECENT developments in blade design techniques can be divided into two families of advanced design tools: the optimization-based approach and the inverse method. In the optimization-based approach, an objective function usually made up of a combination of global quantities with weighting factors is to be minimized (e.g., overall loss, cost, and error in achieving design intent such as total pressure profile).[1,2] Hence, in theory, if properly formulated, the optimization-based method can be very flexible because the design problem can incorporate important design considerations such as off-design performance and multidisciplinary design constraints (e.g., aerodynamic, structure, and cost). However, optimization-based methods are computationally expensive, most existing methods cannot guarantee global optimum solutions, and much work is required to demonstrate the potential of these methods for practical three-dimensional problems. Inverse methods also possess advantages and disadvantages. With inverse methods, the designer needs to prescribe local variables (e.g., blade-surface pressure distributions, blade-surface pressure loading and blade thickness distributions).[3–5] Clearly, it is rather difficult to prescribe local variables that correspond to a global optimum design. The main advantage of inverse method is its computational efficiency in three dimensions.

Inverse techniques for turbomachine blades are being used in industry, but they are not at the sophistication level of the analysis methods.[6,7] Currently, the module used to generate the blade geometry in many design systems are combined throughflow and blade-to-blade quasi-three-dimensional methods.[8] The calculation is first carried out in the meridional plane where the flow is assumed to be axisymmetric using a throughflow matrix method or a streamline curvature method. This step is then followed by the design of the blade profiles on the axisymmetric streamsurfaces using standard families of blade camber surface and thickness distributions, or two-dimensional blade-to-blade inverse methods.[3] Although this family of quasi-three-dimensional blade design modules has been a very useful design tool, it is not satisfactory for some design applications. For example, these methods are not adequate for use in the design of low aspect-ratio blades in highly rotational-flow environments. Here, the presence of strong three-dimensional effects can significantly alter the flowfield (hence the designed blade geometry) modeled by quasi-three-dimensional methods. One example is the three-dimensional oblique shock structure in transonic fans that are treated locally as normal shocks as seen in the meridional plane. Another example is the inability of the quasi-three-dimensional method to model the effects of varying blade stacking accurately (except through the streamtube thickness distribution).

In this paper, we present a fully three-dimensional inverse method that can be used to improve the current quasi-three-dimensional design systems. We propose to retain the existing throughflow methods in an advanced blade design system to accomodate the desire of many design offices to retain these well-established and reliable methods in any blade design system. These throughflow methods can be used to select the work distribution (or design intent) in each blade row. The work distribution is then used by the proposed three-dimensional inverse method as the prescribed flow quantity. The proposed three-dimensional inverse method can replace existing two-dimensional blade-to-blade inverse methods or techniques based on correlations (i.e., standard families of blade camber/thickness distributions and deviation angle correlations) to generate the blade geometry. The inverse method proposed here is an extension of the two-dimensional method summarized in Part 1 (Ref. 9) (for infinitely thin blades) and in a recent paper by Dang[4] (for blades with finite thickness) to three dimensions.

II. Inverse Method

Existing two-dimensional and three-dimensional inverse methods are formulated with different choices of prescribed quantities. The two popular choices are 1) the pressure distributions along the blade upper and lower surfaces,[3,5,10] and 2) the blade pressure-loading distribution (the difference in static pressure between the blade upper

---

Received 2 March 1998; revision received 22 March 2000; accepted for publication 24 April 2000. Copyright © 2000 by the American Institute of Aeronautics and Astronautics, Inc. All rights reserved.

*Associate Professor, Department of Mechanical and Aerospace Engineering.

†Graduate Student, Department of Mechanical and Aerospace Engineering; currently Senior Engineer, Aero/Thermal and Performance, Solar Turbines, Inc., San Diego, CA 92186.

‡Graduate Student, Department of Mechanical and Aerospace Engineering; currently Lead Design Engineer, Compressor Aerodynamic Design, GE Power System, Greenville, SC 29602.

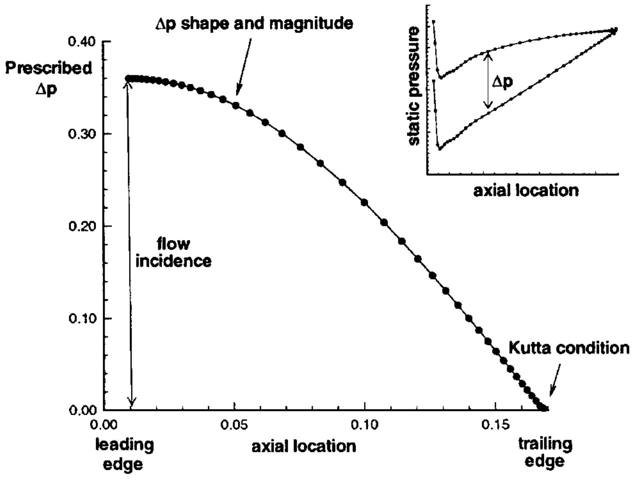

Fig. 1 Prescribed blade pressure loading Δp.

and lower surfaces), a stacking line (in the three-dimensional case), and the blade thickness distribution.[4,11–15] For three-dimensional flows, both approaches have their own advantages and disadvantages. The main issues of concern are the ability to use the method to design blades with improved performance, and the robustness and the ease of integrating the inverse method into existing design systems.

The primary prescribed quantities in this three-dimensional inverse method are the blade thickness distribution, the blade pressure loading distribution $\Delta p(r, z)$, and a stacking line. The computed geometrical quantity is the three-dimensional blade camber surface. The shape of the prescribed blade pressure loading Δp (pressure difference between the blade pressure and suction surfaces) is characterized by the following properties (Fig. 1):

1) The pressure loading must vanish at the blade leading and trailing edges.

2) Flow incidence is imposed by forcing a large gradient in Δp near the blade leading-edge region. We note that with this three-dimensional inverse method, flow incidence is indirectly specified through the loading shape, and blade deviation angle is part of the solution.

The designer must also specify the magnitude of the prescribed Δp distribution. By considering the θ-momentum equation for a control volume coinciding with a streamtube between the blade leading edges (LE) and trailing edges (TE), one can relate Δp to the tangential mass-averaged angular momentum per unit mass $r\bar{V}_\theta$ (Ref. 4):

$$\int r\Delta p \,\mathrm{d}A_\theta = \dot{m}[(r\bar{V}_\theta)_{\mathrm{TE}} - (r\bar{V}_\theta)_{\mathrm{LE}}] \tag{1}$$

where $\dot{m}$ is the mass flow rate within the streamtube. Consequently, the area under the $(r\Delta p)$ vs streamwise-distance curve is approximately related to the local overall change in swirl across a blade row. We note that the right-hand side of Eq. (1) can be approximated using the throughflow solutions by assuming that the blade streamlines coincide with the meridional grid lines.

III. Formulation of the Inverse Problem

In this section, the theory is developed for inviscid flows in three dimensions. The equations to be solved are the standard unsteady Euler equations expressed in terms of the conservative variables. Written in integral form in the cylindrical coordinate system (z, r, θ), the conservation laws take on the form[6]

$$\frac{\mathrm{d}\boldsymbol{U}}{\mathrm{d}t} + \frac{1}{\mathrm{Vol}}\iint_{\mathrm{cell}}[\mathbf{E}\,\mathrm{d}A_z + \boldsymbol{F}\,\mathrm{d}A_r + (\boldsymbol{G} - r\omega\boldsymbol{U})]\,\mathrm{d}A_\theta = \boldsymbol{H} \tag{2}$$

In these equations, ω is the blade rotational speed, Vol is the volume of the cell under consideration, and $(\mathrm{d}A_z, \mathrm{d}A_r, \mathrm{d}A_\theta)$ are the cell boundary surface areas in the (z, r, θ) directions, respectively. The vector $\boldsymbol{U}$ contains the flow variables density, axial, and radial momentum per unit mass, angular momentum per unit mass, and total energy per unit volume, i.e.

$$\boldsymbol{U} \equiv [\rho, \rho V_z, \rho V_r, \rho r V_\theta, e_t]^T \tag{3}$$

The inviscid-flux vectors $(\boldsymbol{E}, \boldsymbol{F}, \boldsymbol{G})$ are defined as

$$\boldsymbol{E} \equiv \left[\rho V_z, \left(\rho V_z^2 + p\right), \rho V_z V_r, \rho V_z r V_\theta, (e_t + p)V_z\right]^T \tag{4}$$

$$\boldsymbol{F} \equiv \left[\rho V_r, \rho V_r V_z, \left(\rho V_r^2 + p\right), \rho V_r r V_\theta, (e_t + p)V_r\right]^T \tag{5}$$

$$\boldsymbol{G} \equiv \left[\rho V_\theta, \rho V_\theta V_z, \rho V_\theta V_r, r\left(\rho V_\theta^2 + p\right), (e_t + p)V_\theta\right]^T \tag{6}$$

and the source vector $\boldsymbol{H}$ is defined as

$$\boldsymbol{H} \equiv \left[0, 0, \left(\rho V_\theta^2 + p\right)/r, 0, 0\right]^T \tag{7}$$

The same flow equations are solved in the analysis and inverse modes. The primary difference in the formulation of these two modes is in the implementation of the boundary conditions along the blade surfaces. In the analysis mode, the usual flow-tangency condition is imposed along the blade surfaces. In the inverse mode, a pressure-jump condition is imposed across the blade surfaces. During the time-marching process of the Euler equations to steady-state, fluid is allowed to cross the blade surfaces, and the flow-tangency conditions along the blade surfaces are used to update the blade shape. When the solution converges, the blade shape is successfully adjusted so that 1) the flow is everywhere tangent to the blade surfaces, and 2) the blade produces the prescribed pressure loading. We note that this type of permeable boundary condition through the blade surfaces during the transient calculation for the blade profile is the same procedure used in Ref. 12, and the procedure has also been used in other time-marching inverse methods.[5,10]

The iterative scheme for the blade profile follows closely the inverse technique developed earlier for blades with finite thickness in two dimensions.[4] The blade surface is periodically updated during the time-marching process of the unsteady Euler equations to steady-state using the flow-tangency conditions along the blade upper surface (superscript +) and the blade lower surface (superscript −):

$$\boldsymbol{W}^{\pm} \cdot \nabla\alpha^{\pm} = 0 \tag{8}$$

Adding and subtracting these conditions yields

$$\boldsymbol{W}^{+} \cdot \nabla\alpha^{+} + \boldsymbol{W}^{-} \cdot \nabla\alpha^{-} = 0 \tag{9}$$

$$\boldsymbol{W}^{+} \cdot \nabla\alpha^{+} - \boldsymbol{W}^{-} \cdot \nabla\alpha^{-} = 0 \tag{10}$$

In these relations, $\boldsymbol{W}$ is the relative velocity defined as $\boldsymbol{W} \equiv \boldsymbol{V} - \omega r\hat{e}_\theta$, and the blade upper and lower surfaces described by the constant $\alpha^{\pm}$ surfaces are defined as[4]

$$\alpha^{\pm} \equiv \theta - (f \pm T/2) = n(2\pi/B) \tag{11}$$

where n is an integer, B is the number of blades, $T = T(z, r)$ is the prescribed tangential blade thickness distribution, and $f = f(z, r)$ is the unknown blade wrap angle distribution in the inverse problem. Following closely the formulation developed earlier,[4] Eq. (9) is used to calculate the unknown blade geometry described by f, i.e.,

$$\langle \boldsymbol{V}\rangle_{\mathrm{bl}} \cdot \nabla f = [\langle V_\theta\rangle_{\mathrm{bl}}/r - \omega] - [\Delta_{\mathrm{bl}}(\boldsymbol{V}) \cdot \nabla T]/4 \tag{12}$$

where the velocity-jump vector $\Delta_{\mathrm{bl}}(\boldsymbol{V})$ and the blade-velocity vector $\langle \boldsymbol{V}\rangle_{\mathrm{bl}}$ are defined as

$$\langle \boldsymbol{V}\rangle_{\mathrm{bl}} \equiv (\boldsymbol{V}^{+} + \boldsymbol{V}^{-})/2 \qquad \Delta_{\mathrm{bl}}(\boldsymbol{V}) \equiv \boldsymbol{V}^{+} - \boldsymbol{V}^{-} \tag{13}$$

Another key quantity which must be formulated for the proposed inverse procedure is the calculation of the blade normal velocity during the iterative process for the blade shape. In the earlier work in two dimensions,[4] it was found that a working algorithm for computing the blade normal velocity is to enforce its tangential component to satisfy the other blade boundary condition given in Eq. (10), i.e.,

$$\Delta_{\mathrm{bl}}(V_\theta) = r[\Delta_{\mathrm{bl}}(\boldsymbol{V}) \cdot \nabla f + \langle \boldsymbol{V}\rangle_{\mathrm{bl}} \cdot \nabla T] \tag{14}$$

Finally, in addition to this formulation for the blade normal velocity, the construction of the fluxes along the blade surfaces must yield the prescribed blade pressure loading Δp.

IV. Numerical Implementation

The iterative process for the blade camber surface $f(z, r)$ consists of marching the unsteady Euler equations to steady-state using an appropriate expression for the blade normal velocity, with the blade camber surface periodically updated using Eq. (12).

A. Flow Equations

In this study, the Jameson–Schmidt–Turkel scheme is used to solve the flow equations.[16] This scheme consists of discretizing Eq. (2) using a finite-volume technique that reduces to a centered-difference approximation on a uniform squared grid. Blended nonlinear second- and fourth-difference artificial dissipation is employed to prevent oscillations in the numerical solutions. The resulting system of ordinary differential equations is then integrated using a four-stage Runge–Kutta time-stepping scheme.

At the inflow and outflow boundaries, boundary conditions are implemented as follows. In the case of subsonic inflow, we specify $(P_{01}, T_{01}, \beta_{r1}, \beta_{\theta 1})$, and we extrapolate the inlet static pressure p_1. In the case of supersonic inflow, we specify $(P_{01}, T_{01}, \beta_{r1}, \beta_{\theta 1}, M_1)$. In the case of subsonic outflow, we specify the back pressure p_2 at the hub or tip and use the radial-equilibrium equation to determine the static pressure at the remaining stations, and we extrapolate for the remaining four primitive variables. Finally, in the case of supersonic outflow, we extrapolate all five primitive variables.

Outside the bladed region, the usual periodic boundary condition is applied along the upper and lower boundaries. In the bladed region, fluid is allowed to cross the blade surfaces during the iterative process for the blade camber surface. Two procedures are developed to evaluate the fluxes through the blade surfaces. The first procedure is based on the blade kinematic condition given in Eq. (14). (Ref. 4) To evaluate the fluxes at the cell faces adjacent to the blades, the density and the z- and r-component velocities along the blade upper and lower surfaces are taken to be the blade values, i.e.,

$$\rho^+ = \rho^- = \langle \rho \rangle_{\mathrm{bl}} \tag{15}$$

$$V_z^+ = V_z^- = \langle V_z \rangle_{\mathrm{bl}}, \qquad V_r^+ = V_r^- = \langle V_r \rangle_{\mathrm{bl}} \tag{16}$$

whereas the θ-component velocity along the blade upper and lower surfaces are evaluated using Eq. (14) (Ref. 4):

$$V_\theta^\pm = \langle V_\theta \rangle_{\mathrm{bl}} \pm [r(\Delta_{\mathrm{bl}}(\boldsymbol{V}) \cdot \nabla f + \langle \boldsymbol{V} \rangle_{\mathrm{bl}} \cdot \nabla T)/2] \tag{17}$$

Finally, the prescribed blade pressure loading Δp is enforced by evaluating the pressure along the blade upper and lower surfaces as follows:

$$p^\pm = \langle p \rangle_{\mathrm{bl}} \pm (\Delta p/2) \tag{18}$$

When the solution converges, the blade profile is aligned with the flow, and the only contributions in the flux vectors $(\boldsymbol{E}, \boldsymbol{F}, \boldsymbol{G})$ at the cell faces adjacent to the blade surfaces are the pressure forces. This condition is correctly imposed through Eq. (18).

The second procedure is based on the compatibility relations derived from the Euler equations, along the line of the approach developed by Demeulenaere and Van den Braembussche.[5] In this approach, the blade upper and lower boundaries are treated as inflow or outflow boundaries, depending on the sign of the transient blade normal velocity. Assuming that the blade normal velocity $W_n^\pm$ is subsonic, there is at least one outgoing wave on the blade upper surface (corresponding to the eigenvalue $W_n^+ - c^+$) and one outgoing wave on the blade lower surface (corresponding to the eigenvalue $W_n^- + c^-$). Along the upper surface, the compatibility relation yields

$$-\bar{\rho}^+ \bar{c}^+ \left(W_n^+\right)^{n+1} + (p^+)^{n+1} = -\bar{\rho}^+ \bar{c}^+ \left(W_n^+\right)^* + (p^+)^* \equiv (C^+)^* \tag{19}$$

Likewise, along the lower surface, it is

$$\bar{\rho}^- \bar{c}^- \left(W_n^-\right)^{n+1} + (p^-)^{n+1} = \bar{\rho}^- \bar{c}^- \left(W_n^-\right)^* + (p^-)^* \equiv (C^-)^* \tag{20}$$

In these relations, the superscript $n+1$ denotes the conditions to be imposed at the new time level, the superscript * denotes the value estimated from the discretization of the Euler equations at the new time level, and the overbar conditions are taken from the old time level. Subtracting Eq. (20) from Eq. (19) yields

$$W_n^{n+1} = \frac{\Delta p^{n+1} - (C^+)^* + (C^-)^*}{\bar{\rho}^+ \bar{c}^+ + \bar{\rho}^- \bar{c}^-} \tag{21}$$

where Δp^{n+1} is the prescribed pressure loading, and we have imposed the condition $W_n^+ = W_n^- \equiv W_n$ taken from Eq. (10). Having calculated the blade normal velocity using Eq. (21), the static pressure along the blade upper and lower surfaces can be computed from Eqs. (19) and (20):

$$(p^+)^{n+1} = \bar{\rho}^+ \bar{c}^+ W_n^{n+1} + (C^+)^* \tag{22}$$

$$(p^-)^{n+1} = -\bar{\rho}^- \bar{c}^- W_n^{n+1} + (C^-)^* \tag{23}$$

These relations ensure that both the compatibility relations given in Eqs. (19) and (20) and the pressure loading condition are satisfied. Numerical experiments show that the second procedure is more robust than the former.

B. Camber Surface Generator and Grid Generation

In the inverse problem, the blade shape is periodically updated during the time-marching process of the flow equations via the camber surface generator given in Eq. (12). The governing equation for the blade wrap angle is of the convective (hyperbolic) type, and a prescribed blade stacking position is given as initial data for this equation. Equation (12) is solved numerically using the Crank–Nicholson scheme.

We note that each time the blade shape is updated, a new computational mesh needs to be generated. To alleviate the grid generation task, a simple sheared H-grid is employed. With this choice of grid topology, the entire three-dimensional mesh can be generated from the meridional mesh and a stretching function that are provided at the beginning of the inverse calculation. The stretching function, denoted by η_k and defined in the range $0 \leq \eta_k \leq 2\pi/B$, is used to generate the mesh point distribution in the θ-direction (B is the number of blades). During the iteration process for the blade wrap angle distribution, the z and r coordinates are fixed (i.e., the meridional mesh), while the θ-coordinate is updated as follows:

$$\theta_{i,j,k} = \pi/B + [1 - (BT_{i,j})/(2\pi)](\eta_k - \pi/B) + f_{i,j} \tag{24}$$

In this expression, we note that only $f_{i,j}$ varies during the iteration process for the blade camber surface. Note that the method can handle blades with thick leading and trailing edges, such as the axial-turbine applications demonstrated in Ref. 4 for an inlet guide vane with a blunt leading-edge and a maximum thickness-to-chord ratio of 25%.

V. Results

A computer program called INV3D was developed and can be used in both the "standard" analysis mode and the inverse mode. The analysis mode of the code was validated using the inviscid version of a NASA code.[6] In terms of coding, the primary difference between these two modes is 1) the subroutine used to evaluate the flux vectors $(\boldsymbol{E}, \boldsymbol{F}, \boldsymbol{G})$ at the cell boundaries next to the blade surfaces (Sec. IV.A) and 2) the addition of a subroutine used to update the blade camber surface and the mesh in the θ direction (Sec. IV.B). A typical inviscid-flow calculation with 100,000 cells running in the analysis mode takes about one hour using a DEC Alpha 21164 533 MHz workstation, whereas an inverse calculation typically takes about 20% more computational time.

In this section, we summarize design studies carried out for a typical transonic fan and a generic supersonic throughflow (STF) fan. The first example illustrates the use of the three-dimensional inverse method to redesign NASA Rotor 67, which is a highly three-dimensional (twisted) blade and has a strong passage shock near the tip region.[17] The second example shows the use of the method to design fan blades that have supersonic axial flow throughout the machine.[18]

A. NASA Rotor 67

In the Rotor 67 design study, the actual geometry definition of the Rotor 67 is used as the baseline design.[17] Because of the inviscid-flow assumption employed here, the mass flow rate is adjusted so that the passage shock near the tip region resides between the blade leading- and trailing-edge (around 3% higher than the actual design mass flow rate). Keeping the blade speed the same as the original design and with no tip clearance, the resulting pressure ratio is around 1.8. At this new design point, the relative inlet Mach number varies from 0.65 at the hub to 1.40 at the tip, with a maximum relative Mach number on the order of 1.75 in the tip region.

We first present the validation study of the INV3D code running in the inverse mode. In this study, we attempt to reproduce the original Rotor 67 geometry using the blade pressure loading Δp computed by an analysis calculation. Figure 2 shows the contour of the blade pressure loading predicted by the INV3D code running in the Euler analysis mode (Fig 2a). This blade pressure loading distribution, along with the blade tangential thickness distribution and the blade stacking line at midchord of the original Rotor 67 design, are used as input to the inverse mode of the INV3D code. The mesh size employed in the inverse calculation is $120 \times 32 \times 24$ cells. Figure 3 shows the comparison of the axial distributions of the blade coordinates (Fig. 3a) and the blade angle (Fig. 3b) at three spanwise locations between the original Rotor 67 geometry and the blade geometry computed by the INV3D code running in the inverse mode. Figure 3 shows that the inverse method successfully reproduces the Rotor 67 geometry.

Next, we present a design modification study of Rotor 67. Figures 4 and 5 show the inviscid solutions of the original Rotor 67 design at the 60 and 90% span locations (Figs. 4a and 5a). The figures include the static pressure contour in the blade-to-blade plane, and the axial distributions of the static pressures along the blade surfaces and the blade pressure loading Δp. The figures show the presence of passage shock waves at these span locations. We observe the presence of two discontinuities (or large gradients) in each of the pressure loading distributions. The first discontinuity corresponds to the passage shock impinging on the blade pressure surface, whereas the second discontinuity corresponds to the passage shock impinging the blade suction surface. These two discontinuities can clearly be seen in the contour plot shown in Fig. 2a. This observation suggests that one can use the inverse method to control the strength/position of the passage shock. For example, the location of the passage shock can be controlled by specifying the discontinuities in the loading shape (or the two legs passage shock) at the desired locations. Also, we expect that a smooth blade pressure loading distribution may correspond to a weak-shock or even a shock-free design.

Figures 4b and 5b show the prescribed pressure loadings of the modified design at the 60 and 90% span locations. The area under the pressure loading curves is kept the same as the original design to ensure that the work distribution remains approximately unchanged [see Eq. (1)]. Note the smoothness in the prescribed loading shapes for the modified design, which can also be seen in Fig. 2b, where the two discontinuities are replaced by much weaker gradients placed near the leading- and trailing-edges. The reader is referred to Ref. 19

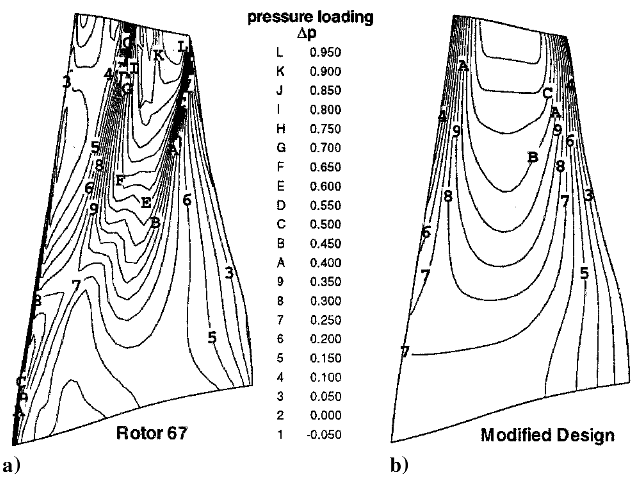

Fig. 2 Comparison of blade pressure loading Δp.

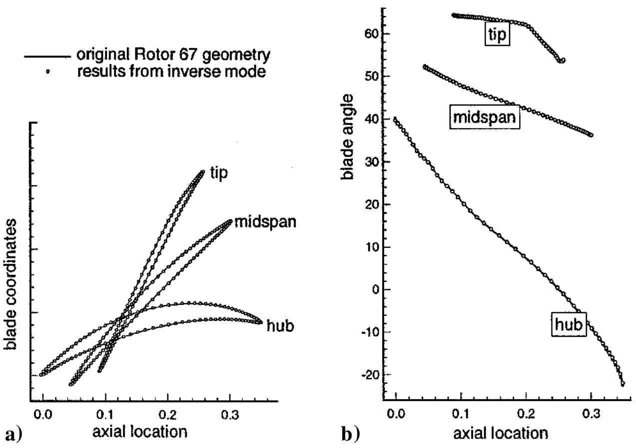

Fig. 3 Consistency check for NASA Rotor 67.

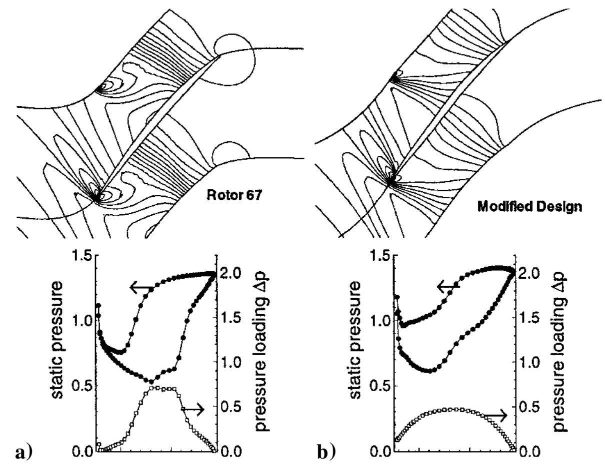

Fig. 4 Flowfield comparison at 60% span location.

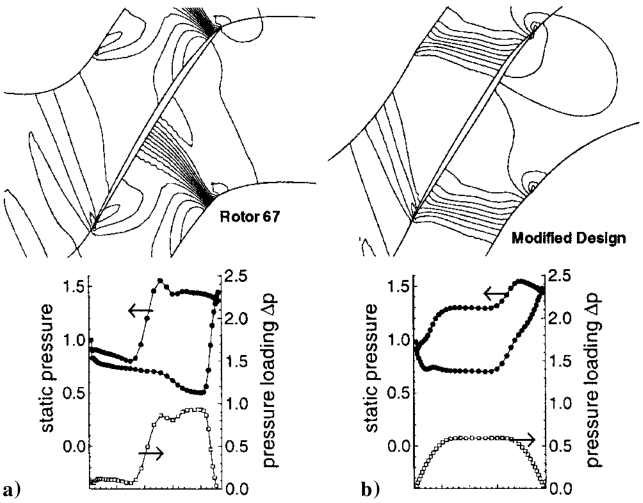

Fig. 5 Flowfield comparison at 90% span location.

for the discussion of the effects of loading shape on the control of shock wave location/strength in the tip region. In Ref. 19, a parametric study carried out with four distinct families of loading shape suggests that the smooth and symmetrical (about midchord) family of loading shapes is the most desirable in terms of 1) forcing the passage shock to reside between the blade leading and trailing edges and 2) weakening the shock. The static pressure plots shown in Figs. 4 and 5 clearly show the weakening of the passage shock. At the 90% span location, the use of a smooth loading shape and the zero incidence design condition has weakened the passage shock considerably (inspection of the entropy plot would confirm this claim). On the other hand, the original Rotor 67 blade has a strong passage shock located near the trailing edge.

Figure 6 gives a comparison of the three-dimensional blade geometries. This figure indicates that the original Rotor 67 blade and the modified blade are very similar, with the latter appearing to have more turning in the hub region. In actuality, the original Rotor 67 design is rear-loaded whereas the modified design is front-loaded, and this difference results in the higher wrap angle for the modified design.

B. STF Fan

A generic STF geometry is used as the baseline design. The hub and shroud geometries, along with the spanwise distribution of the blade axial chord, are similar to those presented in Ref. 18 and are shown in Fig. 7. In this study, the chosen design condition has an inlet axial Mach number of 1.5. The inlet relative Mach number varies from 1.9 at the hub to 2.2 at the tip, and the relative flow angle ranges from −37 deg at the hub to −47 deg at the tip. The design pressure ratio is 2.3. The generic STF fan geometry has a sharp leading edge and is generated using a smooth function, with the leading-edge blade angle set to 5-deg incidence. The blade geometries at the 10 and 90% span locations are shown in Fig. 8 (original STF geometry).

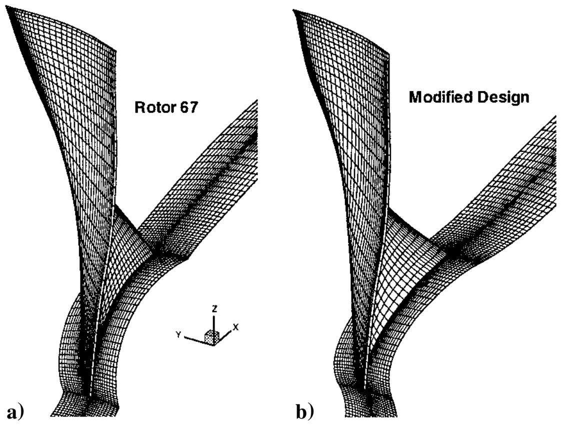

Fig. 6 Comparison of blade geometry.

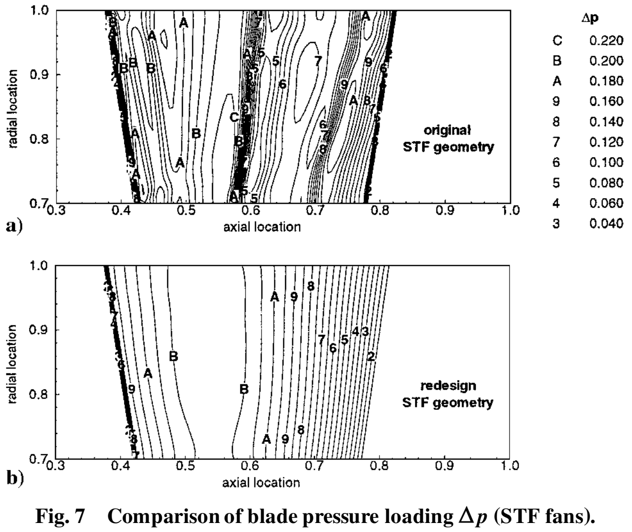

Fig. 7 Comparison of blade pressure loading Δp (STF fans).

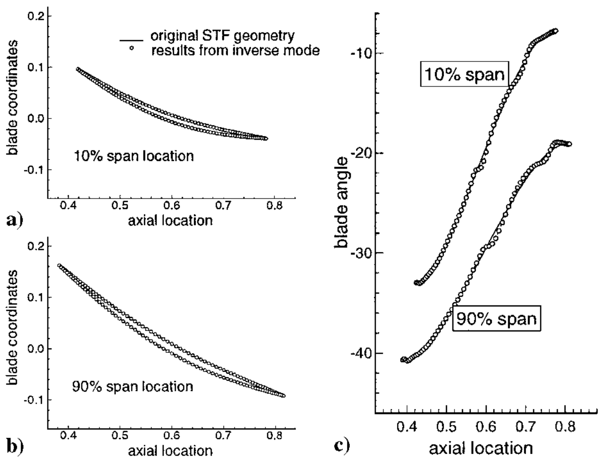

Fig. 8 Consistency check for STF fan.

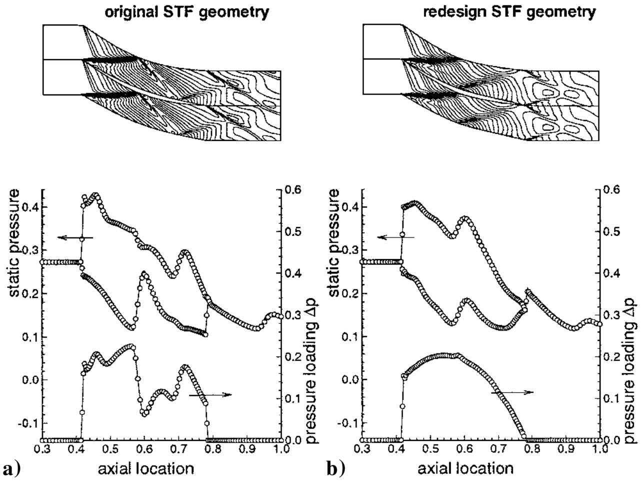

Fig. 9 Flowfield comparison at 10% span location.

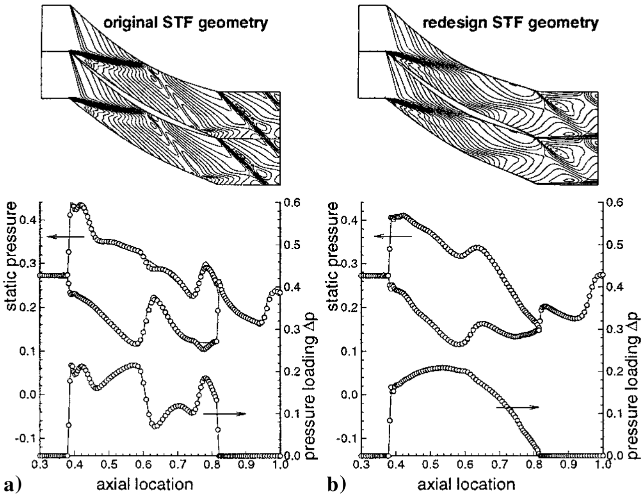

Fig. 10 Flowfield comparison at 90% span location.

As before, we first present the validation study of the INV3D code running in the inverse mode. In this study, we attempt to reproduce the original STF geometry using the blade pressure loading Δp computed by an analysis calculation. Figure 7 shows the contour of the blade pressure loading predicted by the INV3D code running in the Euler analysis mode (original STF geometry). This pressure

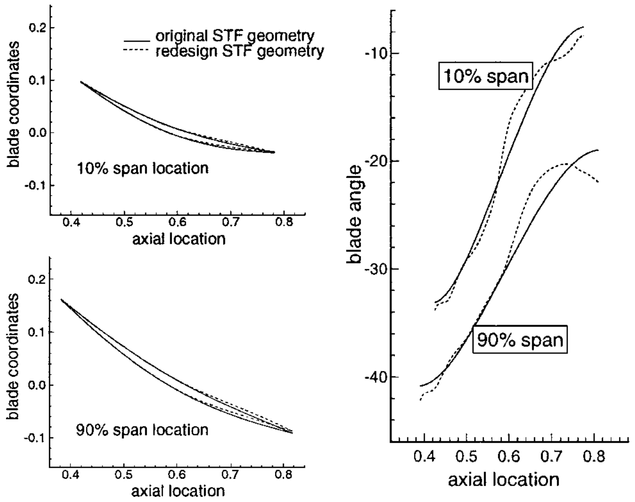

Fig. 11 Comparison of blade geometry (STF fans).

loading distribution, along with the blade tangential thickness distribution and the blade stacking line at midchord taken from the baseline STF geometry, is used as input to the inverse mode of the INV3D code. The mesh size employed in the inverse calculation has 120 × 36 × 24 cells. Figure 8 shows the comparison of the blade geometry and the axial distributions of the blade angle at the hub and tip locations between the original STF geometry and the blade geometry computed by the INV3D code running in the inverse mode. This figure shows that the inverse method successfully reproduces the original STF geometry, although some visible errors are found in the blade angle distributions. We note that this test case is relatively difficult because the shock structure in the blade passage is complex.

Next, we present a design modification study of the STF fan. Figures 9 and 10 show the inviscid solutions of the original STF design at the 10 and 90% span locations (Figs. 9a and 10a). The contour plots show the presence of a complex shock structure in the flow passage, which structure includes 1) the leading-edge oblique shock on the pressure surface and the leading-edge expansion wave system on the suction surface, 2) impinging and reflected shocks in the blade passage, and 3) the trailing-edge shocks. Also shown are the blade-surface static pressure and pressure loading distributions. Observe the four discontinuities in the pressure loading distributions that correspond to the locations of oblique shocks in the blade passage. We will now attempt to redesign the STF geometry so that these shocks are weakened. Assuming that our design problem requires a 5-deg incidence at the leading edge, the leading-edge shock will be present. However, it should be possible to modify the blade goemetry to weaken the reflected shocks along the blade suction surface near midchord and along the blade pressure surface upstream of the trailing edge. Finally, the strong oblique shock at the trailing edge is particularly undesirable because it can trigger shock-induced boundary-layer separation as it impinges on the downstream blade row (the 90% span station is particularly bad). Picking a loading distribution that can weaken the oblique shocks in the blade passage is not obvious. However, it is clear that bringing the loading smoothly to zero in the trailing-edge region should weaken the trailing-edge shock.

Figure 7 (redesign STF geometry) and Figs. 9b and 10b show the contour plot and the x-y plots of the prescribed pressure loading distributions for the redesign STF blades, along with the resulting flowfield. The prescribed loading shape for the redesign STF geometry has a discontinuity at the leading edge that is approximately the same magnitude as the original design. This discontinuity should ensure that the redesign geometry has the same incidence as the original design (roughly 5-deg incidence). Also, the prescribed loading shape for the new design is smooth and is forced to zero at the blade trailing edge. Inspections of the pressure contours in Figs. 9 and 10 show that the most noticeable improvement in the new design is the weakening of the trailing-edge shocks. Another good feature of the new blade geometry is the absence of the reflected shock along the blade suction surface near midchord. Here, the suction surface is bent by the correct amount so that shock cancellation occurs. Since the blade thickness distribution was not modified, the abrupt expansion corner along the blade suction surface produces a compression corner along the blade pressure surface, resulting in the formation of a weak shock wave on the pressure surface. Finally, we note that consistency checks of the calculations are shown in Figs. 9 and 10 as hollow symbols.

Figure 11 gives a comparison of the blade geometries at the 10 and 90% span locations. The figure shows that the two designs are nearly the same in the front portion, but they are noticeably different in the aft portion. The blade angle distributions clearly show the changes near the midchord required to have shock cancellation. These plots also show the reverse camber required to unload the blade smoothly near the trailing edge.

VI. Conclusions

The inverse method for turbomachinery blade design reported in part 1 (Ref. 9) has been successfully extended to three dimensions. In this method, the primary prescribed quantities are 1) the blade pressure loading (i.e., pressure difference between the blade upper and lower surfaces), 2) the blade thickness distribution (including rounded leading and trailing edges of practical interest,[13–15]) and 3) a stacking line. The primary calculated geometrical quantity is the three-dimensional blade camber surface.

In this inverse method, a four-stage Runge–Kutta time-stepping scheme is used to march the finite-volume formulation of the unsteady Euler equations to a steady-state solution. During this time-marching process, fluid is allowed to cross the blade surfaces, and a pressure-jump condition is imposed across the blade surfaces. The blade profile is periodically updated during this time-marching process using the flow-tangency conditions along the blade surfaces. A computer code was developed that can run in both the standard analysis mode and the inverse mode. The computational efficiency of the inverse algorithm is excellent: an inverse calculation typically takes about 20% more computational time than an analysis calculation.

The method is demonstrated for the design of a transonic rotor blade (NASA Rotor 67) and a STF fan. In both test cases, we demonstrated the use of the method to weaken shock waves in the blade passage. The design studies consist of modifying the pressure loading distributions while freezing the blade thickness distribution and a stacking line. These two examples show that blade profiles corresponding to smooth pressure loading distributions tend to have weak shock waves at the design point.

Finally, because of the inviscid-flow assumption employed here, the basic three-dimensional inverse method described in this paper is regarded as a stepping stone toward a practical design tool. The method is being extended to include viscous effects,[13,14] splitter blades,[15] tip-clearance effects, and a multistage capability.

Acknowledgments

This work was supported by the NASA Glenn Research Center (David Miller, Technical Monitor) and AlliedSignal (Arun Sehra, Technical Monitor).

References

[1] Chung, J., and Lee, K. D., "Transonic Compressor Blade Design Using Quasi-3D Navier–Stokes Physics," AIAA Paper 99-2385, June 1999.

[2] Pierret, S., and Van den Braembussche, R. A., "Turbomachinery Blade Design Using a Navier–Stokes Solver and Artificial Neural Network," *Journal of Turbomachinery*, Vol. 121, April 1999, pp. 326–332.

[3] Giles, M. B., and Drela, M., "Two-Dimensional Transonic Aerodynamic Design Method," *AIAA Journal*, Vol. 25, No. 9, 1987, pp. 1199–1205.

[4] Dang, T. Q., "Inverse Method for Turbomachine Blades Using Shock-Capturing Techniques," AIAA Paper 95-2465, July 1995.

[5] Demeulenaere, A., and Van den Braembussche, R. A., "Three-Dimensional Inverse Method for Turbomachinery Blading Design," *Journal of Turbomachinery*, Vol. 120, April 1998, pp. 247–255.

[6] Adamczyk, J. J., Celestina, M. L., Beach, T. A., and Barnett, M., "Simulation of 3D Viscous Flow Within a Multistage Turbine," *Journal of Turbomachinery*, Vol. 112, July 1990, pp. 370–376.

[7] Rhie, C. M., Gleixner, A. J., Spear, D. A., Fischberg, C. J., and Zacharias, R. M., "Developments and Applications of a Multistage Navier–Stokes Flow Solver, Part 1: Multistage Modeling using Body Forces and Deterministic Stresses," *Journal of Turbomachinery*, Vol. 120, 1998, pp. 205–214.

[8] LeJambre, C. R., Zacharias, R. M., Biederman, B. P., Gleixner, A. J., and Yetka, C. J., "Developments and Applications of a Multistage Navier–Stokes Flow Solver, Part 2: Application to a High Pressure Compressor Design," *Journal of Turbomachinery*, Vol. 120, April 1998, pp. 215–223.

[9] Dang, T., and Isgro, V., "Euler-Based Inverse Method for Turbomachine Blades Part 1: Two-Dimensional Cascades," *AIAA Journal*, Vol. 33, No. 12, 1995, pp. 2309–2315.

[10] Wang, Z., Cai, R., Chen, H., and Zhang, D., "A Fully Three-Dimensional Inverse Method for Turbomachinery Blading with Navier–Stokes Equations," American Society of Mechanical Engineers International Gas Turbine and Aeroengine Congress and Exhibition, Paper 98-GT-126, June 1998.

[11] Tan, C. S., Hawthorne, W. R., McCune, J. E., and Wang, C., "Theory of Blade Design for Large Deflections, Part 2: Annular Cascades," *Journal of Engineering for Gas Turbine and Power*, Vol. 106, April 1984, pp. 354–365.

[12] Dang, T. Q., "A Fully Three-Dimensional Inverse Method for Turbomachinery Blading in Transonic Flows," *Journal of Turbomachinery*, Vol. 115, April 1993, pp. 354–361.

[13] Damle, S. V., "Fully Three-Dimensional and Viscous Inverse Method for Turbomachine Blade Design," Ph.D. Dissertation, Dept. of Mechanical Engineering, Syracuse Univ., Syracuse, NY, 1998.

[14] Damle, S., Dang, T., Stringham, J., and Razinsky, E., "Practical Use of Three-Dimensional Inverse Method for Compressor Blade Design," *Journal of Turbomachinery*, Vol. 121, April 1999, pp. 321–325.

[15] Qiu, X., and Dang, T., "3D Inverse Method for Turbomachine Blading with Splitter Blades," American Society of Mechanical Engineers International Gas Turbine and Aeroengine Congress and Exhibition, Paper 00-GT-0526, May 2000.

[16] Jameson, A., Schmidt, W., and Turkel, E., "Numerical Solution of the Euler Equations by Finite Volume Methods Using Runge–Kutta Time-Stepping Schemes," AIAA Paper 81-1259, 1981.

[17] Strazisar, A., Wood, J., Hathaway, M., and Suder, K., "Laser Anemometer Measurements in a Transonic Axial-Flow Fan Rotor," NASA TP 2879, Nov. 1989.

[18] Schmidt, J. F., Moore, R. D., and Wood, J. R., "Supersonic Through-Flow Fan Design," AIAA Paper 87-1746, July 1987.

[19] Dang, T., Nerurkar, A. C., and Reddy, D. R., "Design Modification of Rotor 67 by 3D Inverse Method–Inviscid Flow Limit," American Society of Mechanical Engineers International Gas Turbine and Aeroengine Congress and Exhibition, Paper 97-GT-484, June 1997.

D. S. McRae
Associate Editor